Dynamics studies of high brightness electron beams in a normal conducting, high repetition rate *C*-band injector

A. Giribono[1,*], D. Alesini,[1] F. Cardelli,[1] G. Di Raddo,[1] L. Faillace,[1] M. Ferrario,[1] A. Gallo,[1]
A. Gizzi,[1] S. Lauciani,[1] A. Liedl,[1] L. Pellegrino,[1] L. Piersanti,[1] C. Vaccarezza,[1] A. Vannozzi,[1]
J. Scifo,[1,2] L. Ficcadenti,[3] G. Castorina,[4] G. Pedrocchi,[5] G. J. Silvi,[5] and T. G. Lucas[6]

[1]*Laboratori Nazionali di Frascati, INFN, Via Enrico Fermi, 54 - 00044 Frascati, Italy*
[2]*ENEA - C.R. Casaccia, Dipartimento Fusione e Techologie per la Sicurezza Nucleare,
E Via Anguillarese 301, 00123 Roma, Italy*
[3]*INFN-Roma1, Piazzale Aldo Moro, 2 - c/o Dipartimento di Fisica, 00185 Rome, Italy*
[4]*Università di Catania, Dipartimento Di Ingegneria Elettrica Elettronica E Informatica,
viale A. Doria, 6 95125 Catania, Italy*
[5]*Università La Sapienza, Dipartimento di Scienze di Base e Applicate per I'Ingegneria,
via A. Scarpa 14 00161 Roma, Italy*
[6]*Paul Scherrer Institut, Forschungsstrasse 111 5232 Villigen PSI, Switzerland*

C-band technology is emerging as an exciting innovative approach to the creation of compact new accelerators. Besides the possibility to sustain higher gradients and higher repetition rate operation at normal conducting temperature, it also allows one to increase the machine performance in terms of beam brightness. We propose the design study of a normal conducting, high gradient *C*-band injector aiming at the production of high brightness electron beams—up to 2.6×10^3 TA/m^2—at high repetition rate—up to 1 KHz—as desired to enhance the capabilities of modern radiation sources. This paper reports on beam dynamics studies that guided the injector design looking for a good compromise between the machine compactness and performances. For this purpose, a new standing wave *C*-band gun consisting of 2.6 cells has been designed to enhance the final beam brightness together with its own mode launcher to ensure the needed peak field at the cathode—up to 180 MV/m. Several working points in terms of peak current, transverse emittance and brightness are explored, showing the flexibility allowed by the proposed photoinjector. The integration of the gun mode launcher, that relies on a four-port configuration, in the injector design and its effect on the beam quality are also reported.

I. INTRODUCTION

High brightness electron beams have shown to be essential for the realization of brilliant radiation sources (FEL, inverse Compton sources or THz sources) [1–3] as well as to guide novel acceleration and manipulation schemes based on high gradient wake-fields (plasma accelerators among others) [4]. The 6D brightness, *B*, is defined as:

$$B[\mathrm{A/m^2}] = \frac{Q}{\varepsilon_{nx}\varepsilon_{ny}\sigma_t\sigma_\gamma},\qquad(1)$$

where Q is the beam charge, ε_{nx} and ε_{ny} are respectively the normalized xx' and yy' transverse emittances, σ_t is the bunch length and σ_γ is the energy spread. Thus, a high brightness beam results in a large number of quasimonochromatic electrons, concentrated in very short bunches, with small transverse size and divergence, that is a high particle density 6D phase space.

The rf photoinjectors are established devices in the generation of high brightness electron beams and play a crucial role in the determination of the ultimate beam quality. It is understood that, besides further beam manipulation at higher energy, the main challenge for an rf high brightness photoinjector is generating electron beams with low transverse emittance ($\varepsilon_{nx,y}$ less than 1 mm mrad) and up to kA peak current.

The strength of an rf photoinjector lies in opportunity to explore a wide range of working points in terms of beam parameters. Thus, beam dynamics studies should guide the design of the photoinjector to drive different kinds of devices. For example, one can optimise the peak brightness

for a high brilliance radiation source as an free electron laser (FEL), or the phase space density for a high spectral density ICS source [5], or one can handle the beam length and spot size, both to be set in the μm range, for a plasma-accelerator [6]. Also pump and probe experiments can be performed with wise rf photoinjector setup.

State of the art rf photoinjectors are based on *L* or *S*-band technologies. The breakdown phenomenon limits these technologies from sustaining relatively high accelerating gradients, useful to compact the accelerator machine, and kHz repetition rate operation, particularly desired for high flux modern radiation sources, unless turning to cryogenic temperature system. Out of this effort, the *C*-band technology is emerging as an exciting new approach to the creation of compact new accelerators [7–9]. Besides the possibility to sustain higher gradients and repetition rate operation at normal conducting temperature, it also allows to increase the machine performances in terms of beam brightness [10,11]. The paper is organized as follows: in Sec. II we recall the fruitful technique developed in the years for the electron beam phase space manipulations based on an rf photoinjector; then, in Sec. III, we report on the design study of a normal conducting-high gradient *C*-band injector that would enable the production of high brightness electron beams at high repetition rate—up to 1 KHz—useful for the described applications and in Sec. IV we describe the related dynamics studies for low, medium and high charge electron beams; in Secs. V and VI we describe in details the design of the *C*-band injector, both the standing wave gun and the traveling wave accelerating structures with their solenoids and ancillary components; in Sec. VII we report on the gun feeding system, concerning both the beam dynamics and the gun region design, that have guided the design work flow of the injector. A final summary section is dedicated to conclusions and outlook for the future.

II. HIGH BRIGHTNESS ELECTRON BEAM GENERATION IN RF PHOTOINJECTORS

A photoinjector consists of an rf gun, equipped with a laser driven photocathode system and a solenoid surrounding the gun, that can be followed by one or more accelerating structures as booster section. The electron beam is emitted from the cathode surface, illuminated by a laser pulse, when the applied rf accelerating field overcomes the electric field produced by the electron bunch itself—image and space charge fields. The properties of the photoelectrons arising from the cathode, which depend mainly on the cathode and laser pulse setup, determine the beam intrinsic emittance that represents the lowest beam emittance value one can expect at the photoinjector exit. Once the photoelectrons leave the cathode surface, they undergo external and internal forces through the rf gun that induce emittance oscillations and spoiling the beam quality. In details, the beam transverse beam emittance can be written, assuming no correlation between each term, as the sum in quadrature of the different contributions, that are, the cathode intrinsic emittance, ε_{int}, the cathode surface roughness induced emittance, $\varepsilon_{\text{roughness}}$, the rf induced emittance, ε_{rf}, the space charge emittance, ε_{SC} and the solenoid induced emittance:

$$\varepsilon = \sqrt{\varepsilon_{\text{int}}^2 + \varepsilon_{\text{roughness}}^2 + \varepsilon_{\text{rf}}^2 + \varepsilon_{\text{SC}}^2 + \varepsilon_{\text{solenoid}}^2}. \quad (2)$$

Ideally, it is possible to restore the initial emittance value by properly setting the magnetic field of the solenoid surrounding the gun to counteract the beam internal space charge forces and the external rf kick. If a downstream booster section follows the gun, it is recommended to place it where the beam emittance exhibits its maximum and to set the gun solenoid to satisfy the invariant envelope theory [12] so to let the emittance oscillations damp down to the intrinsic value; that way the beam is quickly pushed up to relativistic energy and the emittance oscillation can be frozen and its minimum at the exit of the accelerating section.

The invariant envelope criteria consists in imposing at the booster entrance a laminar envelope waist ($\sigma'_{x,y} = 0$) with the beam spot size $\sigma_{x,y}$ matched to the accelerating and focusing gradients to stay close to an equilibrium mode

$$\sigma_{x,y} = \frac{1}{k} \sqrt{\frac{I_0}{4\gamma_0 I_A} \left(1 + \sqrt{1 + \left(4\frac{\varepsilon_{nx,y}\gamma_0 k I_A}{I_0}\right)^2}\right)} \quad (3)$$

with $I_A = 17$ kA the Alven current and k the strength of the external focusing channel.

The laser pulse setup is guided by the needed electron beam parameters at the experimental station and by technological constraint in the gun area. Usually it is preferred to set the beam length in the mm range so to reduce the emittance degradation due to the transverse space charge forces before the beam becomes ultrarelativistic. This set point allows for an electron beam with sub mm mrad transverse emittance. Besides further manipulation convenient at high energy—hundreds of MeV—it is also possible to shorten the beam in the photoinjector itself relying on the rf compression in the following rf accelerating structures. This type of compression represents a useful tool to enhance the beam peak current or to tune the beam length, to the experimental station or to a booster linac operating at higher rf frequency, without adding a further longitudinal compression stage. Indeed, once entered the emittance-dominated regime, the insertion of a booster linac at higher operating frequency represents a good practice to boost the beam energy and further shorten the machine taking advantage of the higher accelerating gradient. On the other hand, the energy spread dilution due to rf curvature depends on the bunch length and the accelerating frequency as

$$\frac{\Delta\gamma}{\gamma} \approx 2\left(\frac{\pi f_{\mathrm{rf}}\sigma_z}{c}\right)^2. \tag{4}$$

It follows that the higher the frequency, the shorter the beam should be.

Among other things, the velocity bunching technique permits the compression of the beam inside the first rf structure after the gun and can be integrated in the emittance compensation process [13,14]. It is a longitudinal phase space rotation based on a correlated time-velocity chirp of the electron bunch (electrons in the tail are faster than electrons in the head). If the injected beam is slightly slower than the phase velocity of the rf wave when it is injected at the zero crossing field phase, it slips back to phases where the field is accelerating, being simultaneously chirped and compressed. For soft compression factors one can in principle restore the intrinsic emittance value with the advantage of compactness of the machine and absence of coherent synchrotron radiation (CSR) effects present in a magnetic compressor.

III. THE *C*-BAND PHOTOINJECTOR DESIGN STUDY

The proposed *C*-band photoinjector, designed and simulated at Frascati National Laboratory (LNF), is the result of a long design study carried out in the framework of the CompactLight [15–17], EuPRAXIA@SPARC_LAB [18,19] and IFAST projects [20]. It consists of a 2.6 cells standing wave (SW) gun, with an emittance compensation solenoid, followed by four traveling wave (TW) accelerating structures. The *C*-band TW accelerating structures are 2 m long and can be powered up to 31 MV/m (at 100 Hz repetition rate); the first one is surrounded by a solenoid.

The *C*-band technology has been chosen being a good compromise between the *S* and the *X*-band technology. It enables higher available peak field in the gun region, that results in beam brightness, and higher accelerating gradient in the TW accelerating structures if compared to the *S*-band technology; in the meanwhile it allows larger flexibility as regards the electron beam charge and length if compared to the *X*-band solution. In addition it should ensure a reliable operation at up to 1 kHz repetition rate.

The definition of the photoinjector layout has been guided by the well known wavelength scaling laws [11], which aim to maximise the final beam brightness passing from an rf operating frequency to another. In previous studies [10] the SPARC_LAB photoinjector has been chosen as the starting point being it close to our purposes in terms of electron beam performances and machine setup. In accordance with the scaling laws, it has been roughly halved distances between the elements and their lengths and doubled the electromagnetic field amplitude.

The photoinjector presented in this paper partially breaks with the scaling laws and faces also with technological issues related to the rf components in case of high repetition
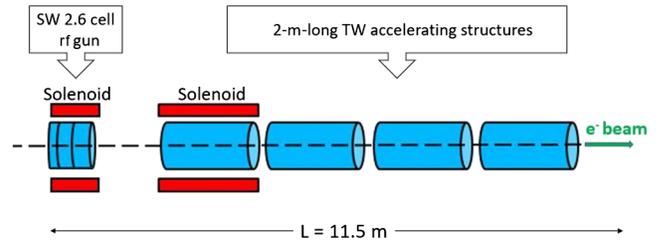

FIG. 1. The *C*-band photoinjector layout, designed and simulated at Frascati National Laboratory (LNF). It consists of a 2.6 cell standing wave gun, with an emittance compensation solenoid, followed by four traveling wave accelerating structures. The TW accelerating structures are 2 m long and can be powered up to 31 MV/m (at 100 Hz repetion rate); the first one is surrounded by a solenoid.

rate operation, i.e., maximum available peak fields, and operational and mechanical needs related to minimum free space between elements for diagnostics, vacuum or others. A huge effort has concerned the design of a new *C*-band gun with its own power distribution system and solenoid as extensively discussed in Secs. V–VII. Indeed, the injector described in [10] relies on a 1.6 cell *C*-band gun operating at least at 240 MV/m peak field, higher than the available one in case of high repetition rate operation—160 MV/m at 1 kHz repetition rate operation. The limitation on the peak field at the cathode forced by the high repetition rate has been overcame by elongating the gun with one more cell so the beam enters the downstream accelerating section with at least 5.5 MeV energy. Likewise, the downstream accelerating sections have been elongated up to 2 m with maximum average gradient of about 31 MV/m. The final layout is closer to a scaled version of the SwissFEL rf gun [21] even if still well integrating the beam dynamics gymnastic performed at the SPARC_LAB facility. In details, it is able to provide electron beams with charges of hundreds of pC, less than 1 mm mrad emittance and hundreds of ampere peak current. It is worth noting that in this configuration, the drift between the booster linac and the cathode plane is 1.7 m long, almost double that of the solution found starting from the SPARC-like case and slightly longer than the PSI scaled solution, making room for the beam characterization after the gun and steering elements before enter in the linac. The final layout is illustrated in Fig. 1.

IV. BEAM DYNAMICS STUDIES

The photoinjector layout has been achieved by comparing several alternative configurations supported by beam dynamics considerations and numerical simulations.

A wide set of working points has been explored in terms of beam charge and bunch length looking at the requirements of the recently proposed European FEL user facilities, such as CompactLight (XLS) or EuPRAXIA@SPARC_LAB (E@S), and of the state of the art ones, taking as reference the SwissFEL performances. The common issue lies in the production of electron beams with brightness of the order of

10^3 TA/m^2 that turns in transverse emittance lower than 1 mm mrad and final kA peak current.

   Three beam charges have been considered with different final rms lengths, obtained by operating the first accelerating section in the on-crest or velocity bunching mode. The rf gun accelerating field ranges between 160 and 180 MV/m and a dephasing of almost 30° between the peak field and the beam allows us to maximize the energy gain in this part, as predicted by analytical calculations [22]. The downstream linac operates in the range 15–31 MV/m to provide the energy tuning in the range 120–260 MeV. A slightly off-crest operation of the second to the fourth accelerating structures, i.e., dephasing of approximately 15° with respect to the maximum rf accelerating field, further reduces the energy spread at the injector exit. On top of that, the beam line matching foresees a proper set of the emittance compensation solenoids and of the accelerating section gradients nearly according to the invariant envelope criteria. The emittance minimization is generally obtained setting the gun solenoid in the range 0.3–0.4 T and the one surrounding the first *C*-band cavity in the range 0.05–0.065 T, depending mainly on the beam charge, the chosen repetition rate (i.e., accelerating peak fields) and the operation mode of the first section, with generally higher gun solenoid and lower section solenoid fields for the case of on-crest operation.

   The bunch distribution at the cathode surface strongly impacts on the optimization process of final parameters at the injector exit. Several computational studies and measurements developed at the SPARC LAB photoinjector have demonstrated that a laser pulse with a flattop longitudinal distribution allows us to minimize the projected emittance value at the injector exit [23]; even better results can be achieved by a tuning of the flattop pulse FWHM duration and rise time [24]. The above considerations, together with an extensive simulation campaign, led to the adoption in the simulations of a photocathode laser pulse with a flattop longitudinal profile with FWHM duration in the picosecond scale and rise time of hundreds of femtoseconds and a transverse uniform distribution of rms spot size (σ_r) of hundreds of micrometers—higher the charge, bigger the spot and the length as predicted by the scaling laws [11]. The laser profile at the cathode surface for the 200 pC beam with final length of 100 μm is reported in Fig. 2 as an example.

   The study has been performed by means of simulations with the multiparticle codes ASTRA [25] and TSTEP [26], which take into account the space charge effects, relevant at very low energies, the beam loading, the coherent synchrotron radiation (CSR) emission and the beam physics near the cathode. The GIOTTO tool [27] has been used in tandem with ASTRA to refine the beam dynamics optimization. In our calculations the cylindrical symmetry of the beam has been assumed to allow us adopting a 2D model, which requires a reasonable number of particles and mesh points, and so
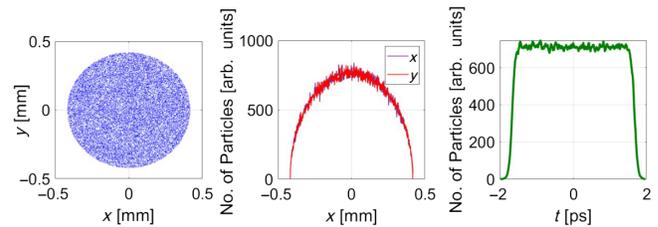

FIG. 2.   Transverse laser spot (left) and horizontal (middle) and longitudinal (right) profiles at the cathode surface for the 200 pC beam with final length of 100 μm.

computational time, with respect to a 3D one. Unless specified, a bunch populated of 30k macro-particles have been considered as a good compromise between reliability and computational time. The intrinsic emittance, ε_{int}, considered to be ≈ 0.60 [mm mrad]/[mm] $\cdot \sigma_r$ [mm rms], has been analytically retrieved scaling the measured value for an *S*-band rf gun operating at peak field at the cathode surface of 120 MV/m [28]. Even if the system relies on relatively high surface field at the cathode, the emittance induced by the cathode surface roughness $\varepsilon_{roughness}$ has been neglected with respect to other contributions being of ≈ 0.005 mm mrad for a peak field at the cathode of 180 MV/m and a nanomachined Cu photocathode. This value has been computed, on the basis of considerations reported in [29], by using the formula [30,31]:

$$\varepsilon_{roughness} = \sigma_x \sqrt{\frac{e\pi^2 a^2 E_{rf} \sin\theta_{rf}}{2m_0 c^2 \lambda}}, \qquad (5)$$

where σ_r is the rms laser spot size, e is the electron charge, E_{rf} is the applied peak field, θ_{rf} is the laser launch rf phase, m_0 is the electron invariant mass and c is the speed of light, a is the amplitude of the uneven surface, and λ is the wavelength of the surface fluctuation.

   Table I lists the working points (WP) described in this paper. The simulations show a machine able to provide beams with up to 1 kA peak current with less than 1.0 mm mrad transverse emittance and up to 250 MeV energy. It has to be noticed that with this machine layout a gentle rf compression factor suffices to get 1 kA peak current without resorting to blowout regime or overcompression schemes that would be instead necessary in case of the use of the *S*-band technology with a consequent worsening of the beam emittance and of the working point stability. The machine performances have been also evaluated in case of low and high repetition rate. As expected, the increase of the repetition rate up to 1 kHz—in place of 100 Hz—mainly results in a limitation on the final beam energy, that goes down to 125 MeV from 250 MeV, and on the beam brightness, with a relative worsening of the 25%, but still complying the mentioned user facility performances. An insight of the listed working follows.

TABLE I. List of the working points described in this paper.

	Low charge		Medium charge			High charge		Units
Charge	75	75	200	200	200	500	500	pC
Average energy	125	105	125	250	200	200	125	MeV
Transverse normalized emittance (100%—rms)	0.15	0.18	0.25	0.25	0.37–0.69	1.3	0.65	mm mrad
Transverse normalized emittance (95%—rms)	0.11	0.13	0.18	0.16	0.25–0.45	0.80	0.44	mm mrad
Length (rms)	380	100	500	500	280–55	55	720	μm
Peak current	20	85	40	40	70–500	1000	70	Ampere
rf compression	off	on	off	off	on	on	off	
Repetition Rate	high	high	high	low	low	low	high	
Peak field @cathode	160	160	160	180	180	180	160	MV/m
TW structure accelerating field	15	15	15	31	31	31	15	MV/m

A. Low charge working point: The CompactLight case study

The CompactLight collaboration is studying an X-band linac-based FEL radiation source with wavelengths ranging from infrared to x-rays. The X-band linac will be driven by the described normal conducting—high gradient C-band injector operating at up to 1 KHz rep rate and is equipped with two magnetic compression modules (chicane) to provide a 5 kA peak current beam at the undulator entrance with less than 0.2 mm mrad rms transverse emittance.

The reference working point for the XLS case study foresees a 75 pC electron beam that reaches the X-band linac entrance with 0.11 mm mrad transverse normalized emittance, 400 μm length and 125 MeV energy. For this purpose, the photoinjector is operated on-crest nearly according to the invariant envelope criteria as to compensate the transverse beam emittance with a deviation of the 5% from the intrinsic one.
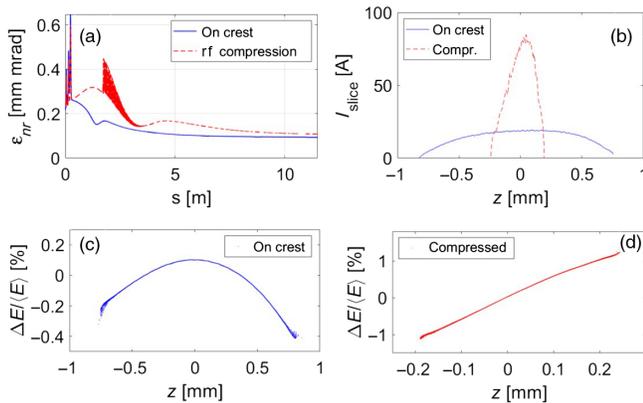

FIG. 3. Evolution of the transverse normalized emittance (a) and slice peak current (b) for the on crest (blue line) and for the compressed beam (red dashed-line) and the longitudinal phase space at the photoinjector exit for the on crest (c) and the compressed beam (d).

The generation of much shorter electron beams—almost 100 μm—in the photoinjector by means of the velocity bunching technique has been also investigated in order to mitigate the rf curvature effects on the beam longitudinal phase space due to a much longer beam in the X-band linac as described by Eq. (4).

Both the described WP show similar performances in terms of transverse emittance with a peak current ranging between 20 and 85 A. Indeed, thanks to the velocity bunching one can increase the peak current of a factor four with a relatively tolerable deterioration of the rms transverse emittance (12.5%). Moreover, this scenario is attractive also because it allows one to relax the magnetic chicane performances, so to mitigate the CSR effects on the transverse phase space, and acts as a longitudinal phase space linearizer. The simulation results are reported in Table I and in Fig. 3. Figure 3 shows the evolution of the transverse normalized emittance (a) and slice peak current (b) for the on crest (blue line) and for the compressed (red dashed-line) beams and longitudinal phase space at the photoinjector exit for the on crest (c) and the compressed beams (d).

B. Medium charge working point: The EuPRAXIA@SPARC_LAB case study

The EuPRAXIA@SPARC_LAB collaboration is preparing a technical design report for a multi-GeV plasma-based accelerator with outstanding electron beam quality to pilot an x-ray FEL, the most demanding in terms of beam brightness. The plasma-based accelerator is operated in the external injection beam driven configuration by means of an rf injector consisting of an S-band, high brightness photoinjector followed by an X-band booster linac embedded with a magnetic chicane for longitudinal compression at high energy. The S-band technology has been chosen being the current state of the art with stable and reliable performances in terms of beam brightness. The upgrade of the S-band

photoinjector with a *C*-band one is actually ongoing in order to compact the machine and increase the beam brightness.

The main EuPRAXIA@SPARC_LAB working point relies on an electron beam with one GeV energy, less than 1 mm mrad transverse emittance and at least 1.5 kA peak current at the undulator entrance. The beam energy will be boosted up to one GeV by using the *X*-band linac coupled or not with the plasma acceleration module, depending on the type of application as reported in [32]. For these purposes the plasma accelerator requires for a so-called comb-beam, a 200 pC—55 μm long beam (the driver) followed by a 30 pC–3 μm long beam (the witness), while the full *X*-band linac option (without the plasma) requires instead for a single bunch with charges in the range 200–500 pC and rms length of the order of 100 μm. In both cases the photo-injector will be operated in the velocity bunching configu-ration with different compression regime.

The beam dynamics has been studied to generate a 200 pC beam with a variable length in the range 55–280 μm. In details, three beam length have been investigated, 55, 100, and 280 μm, the first one of interest as driver of a particle wake field acceleration accelerator and the following ones representing the maximum lengths to avoid distortions of the longitudinal phase space in a downstream X or *C*-band booster linac, respectively. For the sake of completeness the on-crest operation has been investigated resulting in electron beam performances very close to the SwissFEL facility considering both the high and low repetition rate, see Table I. The results are reported in Figs. 4 and 5. Figure 4 reports the behavior of the transverse normalized emittance versus the beam peak current for different beam charges. The numerical studies confirm the predictions of the scaling laws discussed in Sec. III. Figure 5 illustrates the slice analyzes of the transverse normalized emittance and of the peak current for different compression factors in case of velocity bunching operation in comparison with the on-crest operation. The VB 1 to 3 are related to the case with final bunch length of 280, 100, and 50 μm, respectively.
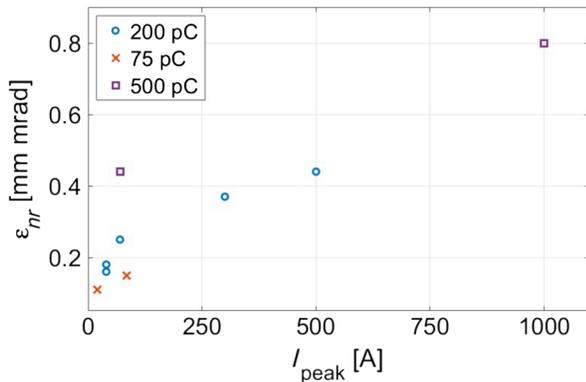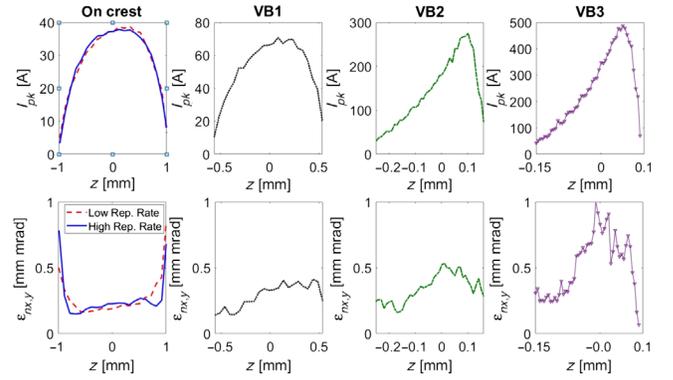

FIG. 5. Slice analyses of the transverse normalized emittance and of the peak current for different compression factors in case of velocity bunching operation. The VB 1 to 3 are related to the case of final beam length of 280, 100, and 50 μm, respectively.

C. High charge working point

For the sake of completeness, beam dynamics studies have been expanded to include a high-charge beam case. The dynamics of a 500 pC beam has been investigated resulting in rms beam length in the range 55–750 and rms transverse emittance less than 1 mm mrad. This type of beams find applications as drivers of high flux light sources described in literature, such as the inverse Compton sources [33,34] and of the THz source [35], but also as drivers of plasma accelerators to heighten the accelerating gradient, that depends on the driver beam charge, as recently proven at SPARC_LAB.

V. THE *C*-BAND GUN

The gun is a 2.6-cell standing wave (SW) structure operating with a peak field (E_{cath}) at the cathode of 160–180 MV/m. It has been designed to set the coupling coefficient equal to 3 so to allow the operation with short rf pulses ($\tau_{rf} < 300$ ns) to reduce the breakdown rate (BDR), the pulsed heating [36], and the power dissipation [37]. An elliptical profile of the iris with large aperture (diameter of 18 mm) has been also implemented to reduce the peak surface electric field and the modified Poynting vector [38], to increase the frequency separation with the nearest $\pi/2$ mode and to have a better pumping on the cathode cell. A four-port mode launcher [39,40] with an on-axis coupling has been adopted to reduce the pulsed heating on the coupler and to perfectly compensate the dipole and quadru-pole field components [41].

The electromagnetic design has been performed using ANSYS HFSS [42]. The simulated gun geometry and the magnitude of the electric field is reported in Fig. 6. It has to be noticed that the mode launcher design also includes two pumping ports. Figure 7 illustrates amplitude and phase of the longitudinal electric field along the beam propagation axis also including the mode launcher region, where the field presents a traveling wave component (nonconstant

FIG. 4. Behavior of the transverse normalized emittance versus the beam peak current for different beam charges.
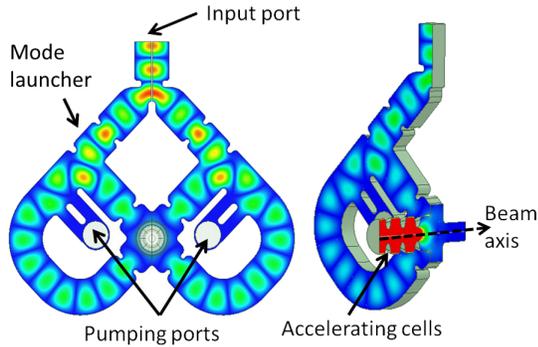
FIG. 6. Electromagnetic design of the gun and magnitude of the electric field as obtained by means of ANSYS-HFSS simulations.
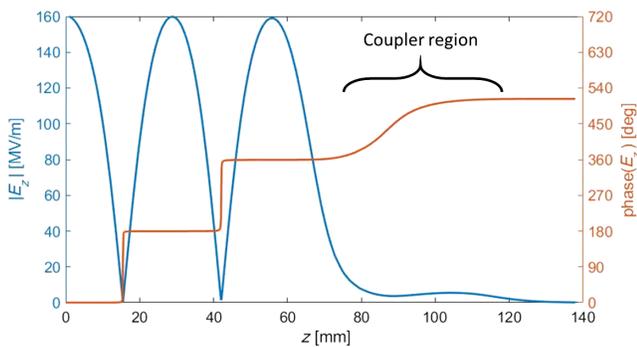

FIG. 7. Amplitude and phase of the longitudinal electric field along the beam propagation axis. The plot also includes the mode launcher region, where the field presents a traveling wave component (nonconstant phase) related to the power flow into the gun.
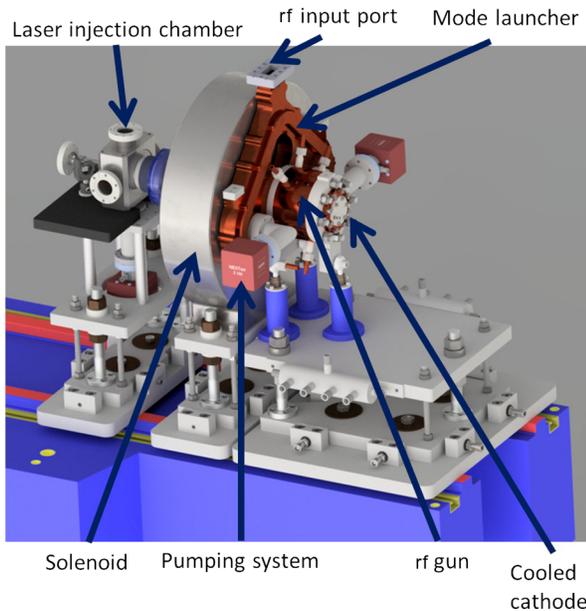

FIG. 8. Three dimension mechanical drawing of the entire gun region, also including essential components as the pumping system, the solenoid and the laser injection chamber.

TABLE II. Main gun parameters for the 100 Hz operation rate and for the 400 Hz repetition rate (in parenthesis), the latter being the maximum operation rate for available commercial klystrons [43].

Working frequency (GHz)	5.712
$E_{cath}/P_{diss}^{1/2}$ [MV/(mMW$^{1/2}$)]	51.4
rf input power (MW)	23 (18)
Cathode peak field (MV/m)	180 (160)
Cathode type	copper
Rep. rate (Hz)	100 (400)
Quality factor	11900
Filling time (ns)	166
Coupling coefficient	3
rf pulse length (ns)	300
E_{surf}/E_{cath}	0.96
Modified Poynting vector (W/μm^2)	3.2 (2.5)
Pulsed heating (°C)	20 (16)
Average diss. Power (W)	320 (1000)

phase) related to the power flow into the gun. The insertion of the mode launcher has opened to an increased flexibility in positioning the input waveguide relative to the gun body that results in a more powerful cooling capability of the accelerating cells especially useful in the high repetition rate operation. A careful design of the cooling system has been performed to avoid the detuning of the gun during the operation and a nonuniform cell deformations, that results in an unbalanced accelerating field along the gun [41]. To this purpose, the gun integrates four cooling channels: three for the accelerating cells and one for the cathode. The 3D model of the gun, including the cooling system, has been implemented in ANSYS Workbench environment and a full coupled thermal, structural, and electromagnetic analysis, has been performed showing the capability of the device to sustain the high repetition rate operation [37,41]. The C-band gun realization and test has been funded by the EU in the framework of the I.FAST project [20] and by INFN Commission V. The power test are on-going. Figure 8 reports the mechanical drawing of the entire gun region, also including essential components such as the pumping system, the solenoid and the laser injection
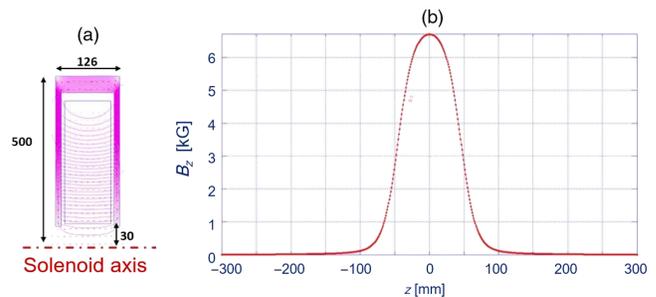

FIG. 9. (a) Solenoid geometry (dimensions are in mm) and (b) the on-axis magnetic field as obtained by means of Poisson-Superfish simulations.

TABLE III.   Main gun solenoid parameters.

B_{max} (T)	0.79
Bore radius (mm)	30
Solenoid length (mm)	126
Yoke material	Low Carbon Steel
Integrated field (T mm)	64.5
Good field region radius (mm)	10 mm
Integrated field variation	3×10^{-5}
Number of turns	280
Conductor dimension (mm)	6×6/bore 4
Nominal current (A)	184
Nominal voltage (V)	6
Inductance (mH)	3
Resistance (mΩ)	178
Water flow rate (l/min)	4.5
Temperature drop (°C)	18
Pressure drop (bar)	3

FIG. 10.   Schematic layout of the *C*-band booster feeding system.

chamber. The detailed description of the gun design, thermo-mechanical analysis and rf measurements are out the scope of the present paper and will be the subject of a dedicated paper.

The gun parameters are reported in Table II for 100 Hz operation rate and for 400 Hz repetition rate, denoted in parenthesis, the latter being the maximum operation rate for available commercial klystrons [43]. Based on these considerations, all the calculations have been carried out taking into account this realistic scenario, while the 1 kHz operation rate has been considered as a possible future upgrade of the mentioned power sources [44].

The gun solenoid, that allows one to control the beam emittance oscillations and to match the beam to the downstream accelerating structures, as widely discussed in the previous sections, is a 12 cm long device consisting in a single coil with a bore radius of 3 cm. It has been designed by using the Poisson Superfish [45] code. Figure 9 shows the solenoid geometry (a) and the on-axis magnetic field (b) as obtained by means of Poisson-Superfish simulations. The main gun solenoid parameters are reported in Table III.

VI. *C*-BAND TRAVELING WAVE ACCELERATING STRUCTURES

The *C*-band traveling wave module is made up of four 2 m long traveling wave accelerating structures fed by one klystron and one pulse compressor. The schematic layout of the feeding system is given in Fig. 10. The *C*-band structure parameters are listed in Table IV and they have been found using the same algorithm illustrated in [46]. Each structure has a linear tapering of the irises. The average dimension of the iris ($\langle a \rangle$) and the tapering angle have been chosen in order to maximize the structure efficiency. We have considered the klystron parameters listed in Table V that
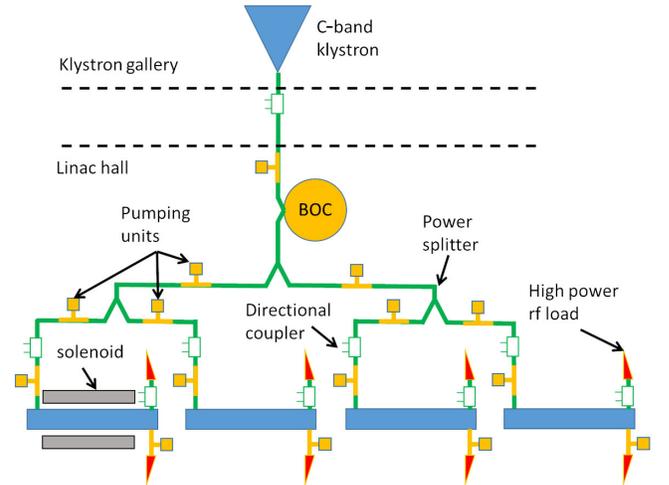
are referred to commercial klystrons [43] and the BOC pulse compressor parameters are those already implemented for the Swissfel [47].

A. *C*-band structure solenoid

The solenoid around the first accelerating structure, essential for the beam emittance compensation in velocity bunching a solenoid, has been designed using the Poisson

TABLE IV.   Main parameters of the *C*-band structures (in parenthesis we have reported the 400 Hz repetition rate case).

Working frequency (GHz)	5.712
Phase advance per cell (rad)	$2\pi/3$
Average iris radius $\langle a \rangle$ (mm)	6.6
Iris radius **a** (mm)	6.94-6.26
Number of cells per structure	120
Accelerating cell length (mm)	16.67
Structure length $\mathbf{L}_s$ (m)	2
Shunt impedance **R** (MΩ/m)	71–77
Effective shunt impedance $\mathbf{R}_s$ (MΩ/m)	190
Group velocity v_g/c (%)	2.4–1.6
Filling time (ns)	336
Average acceleration gradient (MV/m)	31 (15)
Required input power per module (MW)	41 (9)
Number of structure in the module	4

TABLE V.   Main parameters of the *C*-band klystron.

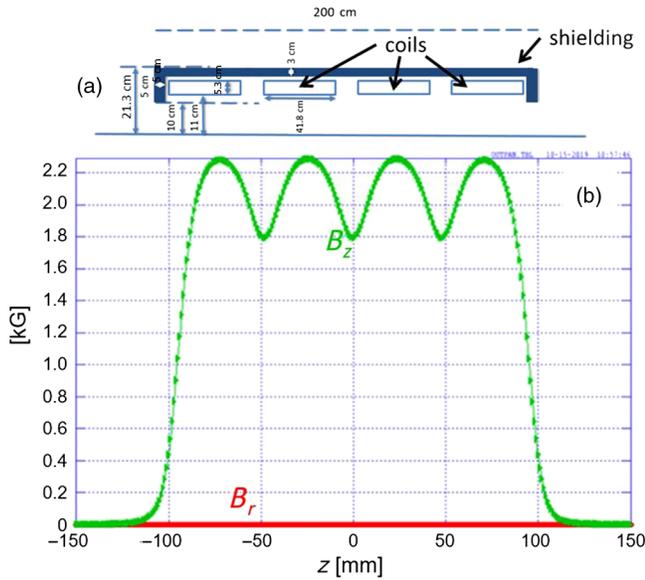|	
Operating frequency (GHz)	5.712
Klystron pulse length (μs)	2
Klystron peak power (MW)	15
Repetition rate (Hz)	400
Q_0 of BOC	216000
Q_E of BOC	19100

FIG. 11.　(a) Geometry of the C-band solenoid simulated with Poisson-Superfish (dimensions are in mm); (b) longitudinal (B_z) and radial (B_r) magnetic field on axis.

Superfish [48] code. It is composed of four coils embedded in an iron shielding. Figure 11 shows the simulated geometry (a) and the profile of the on-axis magnetic field (b).

VII. BEAM DYNAMICS STUDIES IN CASE OF MODE LAUNCHER WITH CIRCULAR WAVEGUIDE

In the machine layout described so far, the rf gun is fed by a mode launcher placed downstream the gun itself and consequently the gun solenoid is moved relatively far away from the cathode. Indeed, the gun solenoid is generally placed as close as possible to the cathode so to avoid the increase of the beam emittance in and immediately after the gun region. The solution above described, represents a trade-off between beam dynamics considerations and radio-frequency feeding system requirements.

Another solution for the feeding system, devoted to maximize the electron beam performances in terms of emittance and peak current, is described in [17]. In this case, the rf gun is fed by a mode launcher placed downstream the gun solenoid through a circular wave-guide. Even if this configuration permits one to place the gun solenoid closer to the cathode, the electromagnetic design results much more complicated and presents two main drawbacks: a residual counterpropagating e.m. field in the circular wave-guide, that interacts with the electron beam in the downstream drift, and a higher residual magnetic field at the cathode due to the need of a bigger bore of the gun solenoid, that leads to the beam emittance growth [49] as predicted by the Busch's theorem [50]. The latter has been mitigated in this solution, thanks to the insertion of a bucking coil behind the gun. Figure 12 illustrates the
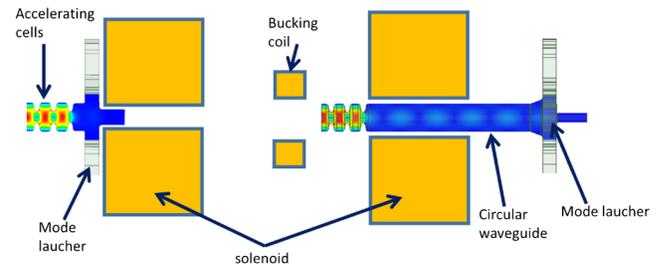

FIG. 12.　Schematic layout of the gun feeding system. Two solutions have been considered: a solution with a mode launcher placed upstream the gun solenoid (left) and a solution with a mode launcher placed downstream the solenoid together with a circular wave-guide (right).

schematic layout of the two solutions: the one with the mode launcher placed upstream the gun solenoid on the left and the one with the mode launcher placed downstream the solenoid, together with the circular wave-guide, on the right.

For the sake of completeness, the electromagnetic and beam dynamics studies performed for the latter solution are described in the following sections. The gun has been designed using the ANSYS HFSS code [42] and the solenoid, described in [51], has been designed using Poisson Superfish. The simulated gun geometry and the magnitude of the electric field is reported in Fig. 13. Table VI reports the specifications of the solenoid embedded with the bucking coil and Fig. 15 illustrates the solenoid geometry (a) and the on-axis magnetic field profile (b) with the bucking coil switched on (red line) and off (blue dashed line) as obtained by means of Poisson Superfish simulations. Figure 14 illustrates the on-axis e.m. field profile in the gun region: it has to be noticed that the
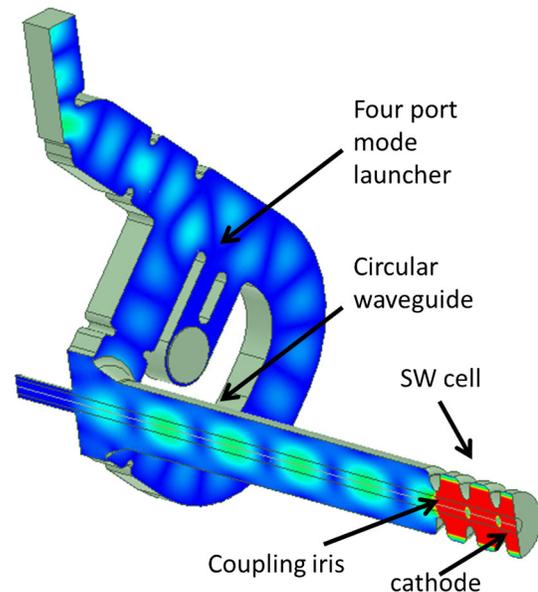

FIG. 13.　Gun geometry with the circular wave-guide as result of ANSYS-HFSS simulations.

TABLE VI. Main gun solenoid equipped with bucking coil parameters.

Solenoid specifications	
B_{max} (T)	0.5285
Yoke material	Low Carbon Steel
Total integrated field (T mm)	59.4
Good field region radius (mm)	10 mm
Integrated field variation	3^{-5}
Number of turns per coil	336
Conductor dimension (mm)	5.6×5.6/bore 3.6
Nominal current per coil (A)	164
Nominal voltage per coil (V)	40
Inductance per coil (mH)	3
Resistance per coil (mΩ)	242
Water flow rate per coil (l/min)	3.72
Temperature drop per coil (°C)	25
Pressure drop per coil (bar)	2.72

Bucking coil specifications	
Conductor diameter (mm)	1.6
Number of turns	700
Nominal current (A)	7.5

field is standing wave in the gun while it is traveling wave (nonconstant phase) and counterpropagating (positive slope of the phase) in the circular wave-guide because of the power flow from the mode launcher into the gun itself.

The effects of the residual traveling wave component in the mode launcher region on the beam dynamics have been detailed investigated by means of simulations with the ASTRA code. The simulations have been performed implementing the 3D routine, for both the space charge tracking and the modeling of static and electromagnetic elements, and a user-defined modeling of the gun and its input power
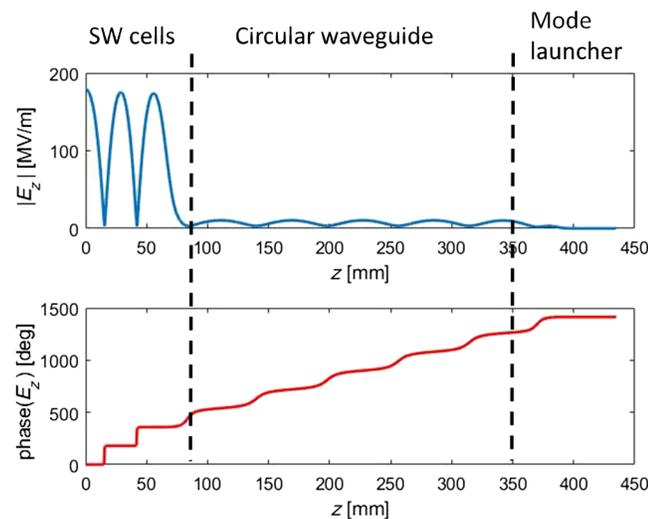

FIG. 14. Longitudinal electric field on axis with the circular wave-guide as result of ANSYS-HFSS simulations.
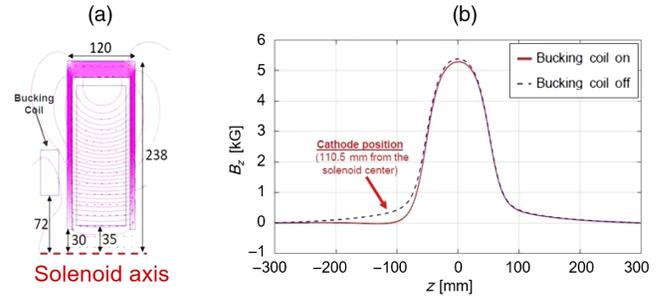

FIG. 15. (a) Solenoid geometry (dimensions are in mm) and (b) on-axis magnetic field profile with the bucking coil switched on (red line) and off (blue dashed line) as obtained by means of Poisson-Superfish simulations.

region, without any assumption on the field temporal evolution (nor TW nor SW), by combining the real and imaginary parts of the e.m. fields.

The study has been performed in terms of the evolution of the main beam parameters taking as reference the XLS case study with a 3D modeling of the gun without the mode launcher. This reference case has been also used to reduce the main numerical error contributions of the 3D HFSS simulations, i.e., the discontinuities and numerical noise of the electromagnetic maps, on the beam dynamics ones. In order to bring them down it has been properly defined the HFSS resolution step size and tetrahedral edge of the simulation and the extraction data setting.

A. Longitudinal beam dynamics

The longitudinal beam dynamics has been studied by means of both numerical integration methods and simulations. The main contribution lies in the oscillation of the beam energy around a mean value caused by the fluctuations of the longitudinal component of the fields in the mode launcher region. Figure 16 illustrates the beam energy evolution in the gun region with (red) and without (blue) the insertion of the mode launcher calculated by
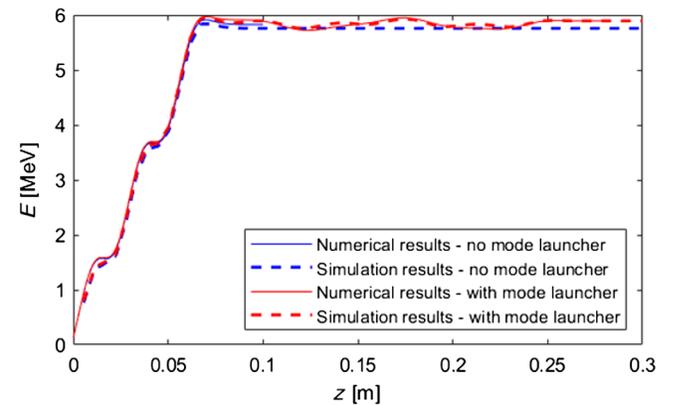

FIG. 16. Beam energy evolution in the gun region with (red) and without (blue) inserting the mode launcher calculated by means of the numerical integration method (lines) and simulations (dashed-lines).
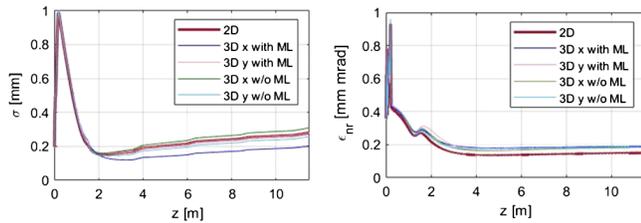
FIG. 17. Evolution of the beam transverse spot size (left) and emittance (right) through the injector with and without the insertion of a coaxial mode launcher.

means of the numerical integration method (lines) and simulations (dashed-lines).

B. Transverse beam dynamics

The transverse beam dynamics has been studied by using 3D field-maps in order to avoid any assumption of the cylindrical symmetry of the mode launcher. The residual numerical noise of the 3D field maps can lead to fictitious contributions to the beam quality in terms of transverse beam asymmetry and emittance increase. At first, simulations have been performed in case of a cylindrical symmetric gun geometry with and without a coaxial mode launcher in order to quantify and distinguish the magnitude of the beam quality worsening due to the numerical noise and to the mode launcher insertion. Figure 17 illustrates the evolution of the beam transverse spot size (left) and emittance (right) through the injector with and without the insertion of the mode launcher (ML). Looking at these figures one can conclude that the beam quality deterioration is mainly due to the residual numerical noise of the field maps. In detail, the observed emittance increase is relatable to the map discontinuities, while the artificial asymmetries have been reduced working on the tetrahedral edge size of the HFSS simulations (the best value for Δ is 0.5 mm).

Different configurations have been considered for the mode launcher. The final layout relies on a fully symmetric four port waveguide mode launcher as to avoid spurious and unwanted quadrupolar components of the field. Figure 18 illustrates the evolution of the beam transverse spot size (left) and emittance (right) through the injector with the insertion of a coaxial (red lines) and a four port (blue lines) mode launcher. The study suggests that the
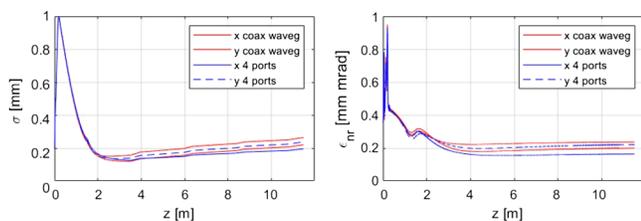

FIG. 18. Evolution of the beam transverse spot size (left) and emittance (right) through the injector with the insertion of a coaxial (red lines) and a four port (blue lines) mode launcher.

effect on the beam quality is not quantifiable and that one can account for a complete recovery of the beam quality by suppressing the numerical noise or by inserting some skew quadrupoles just after the gun, if still needed.

VIII. CONCLUSIONS

The requirement for the latest generation of light sources, is the capability to delivery high-intensity photon beams with a high level of brightness and quality, providing large scenery for science applications. The starting point to obtain a suitable electron beam for these applications is to have a proper photoinjector, a key device to produce the high brightness electron beams required for the realization of a brilliant radiation sources. In this framework, the design of a C-band compact high-brightness photoinjector integrates perfectly into a wide scenario that includes present and next future photon source facilities. The design and the beam dynamics optimization has been detailed described pointing out on the essential condition needed for obtaining electron beams with up to kA peak current and sub mm mrad transverse normalized emittances. The resulting machine is a very flexible tool able to meet the needs of the next light sources with very different characteristics and to improve the performances of the existing ones.

ACKNOWLEDGMENTS

[1] N. Huang, H. Deng, B. Liu, D. Wang, and Z. Zhao, Features and futures of x-ray free-electron lasers, Innovation **2,** 100097 (2021).

[2] V. Petrillo, I. Drebot, M. Ruijter, S. Samsam, A. Bacci, C. Curatolo, M. Opromolla, M. R. Conti, A. R. Rossi, and L. Serafini, State of the art of high-flux compton/thomson x-rays sources, Appl. Sci. **13,** 752 (2023).

[3] S. S. Dhillon *et al.*, The 2017 terahertz science and technology roadmap, J. Phys. D **50,** 043001 (2017).

[4] C. Emma, J. Van Tilborg, R. Assmann, S. Barber, A. Cianchi, S. Corde, M. E. Couprie, R. D'Arcy, M. Ferrario, A. F. Habib *et al.*, Free electron lasers driven by plasma accelerators: status and near-term prospects, High Power Laser Sci. Eng. **9,** e57 (2021).

[5] A. Bacci *et al.*, Electron linac design to drive bright compton back-scattering gamma-ray sources, J. Appl. Phys. **113,** 194508 (2013).

[6] E. Chiadroni *et al.*, Beam manipulation for resonant plasma wakefield acceleration, Nucl. Instrum. Methods Phys. Res., Sect. A **865,** 139 (2017).

[7] L. Faillace, R. Agustsson, M. Behtouei, F. Bosco, D. Bruhwiler, O. Camacho, M. Carillo, A. Fukasawa, I. Gadjev, A. Giribono, L. Giuliano, S. Kutsaev, N. Majernik, M. Migliorati, A. Mostacci, A. Murokh, L. Palumbo, B. Spataro, S. Tantawi, C. Vaccarezza, O. Williams, and J. B. Rosenzweig, High field hybrid photo-injector electron source for advanced light source applications, Phys. Rev. Accel. Beams **25**, 063401 (2022).

[8] R. R. Robles, O. Camacho, A. Fukasawa, N. Majernik, and J. B. Rosenzweig, Versatile, high brightness, cryogenic photoinjector electron source, Phys. Rev. Accel. Beams **24**, 063401 (2021).

[9] R. Zennaro, J. Alex, M. Bopp, H. Braun, A. Citterio, H. Fitze, M. Pedrozzi, and J.-Y. Raguin, Conceptual design of the c-band module for swissfel, in *Proceedings of the 25th International Linear Accelerator Conference, LINAC2010, Tsukuba, Japan* (JACoW, Geneva, Switzerland, 2010).

[10] M. Croia, D. Alesini, F. Cardelli, M. Diomede, M. Ferrario, A. Giribono, S. Romeo, C. Vaccarezza, and A. Vannozzi, High gradient ultra-high brightness *C*-band photoinjector optimization, J. Phys. Conf. Ser. **1596**, 012031 (2020).

[11] J. Rosenzweig and E. Colby, Charge and wavelength scaling of RF photoinjector designs, AIP Conf. Proc. **335**, 724 (1995).

[12] L. Serafini and J. B. Rosenzweig, Envelope analysis of intense relativistic quasilaminar beams in rf photoinjectors: A theory of emittance compensation, Phys. Rev. E **55**, 7565 (1997).

[13] B. Aune and R. H. Miller, New method for positron production at Slac, in *Proceedings of the Linear Accelerator Conference, Montauk, NY*, edited by R. L. Witkover (Brookhaven National Laboratory, Upton, New York, 1980), pp. 0–3.

[14] M. Ferrario *et al.*, Experimental Demonstration of Emittance Compensation with Velocity Bunching, Phys. Rev. Lett. **104**, 054801 (2010).

[15] S. Di Mitri *et al.*, Scaling of beam collective effects with bunch charge in the CompactLight Free-Electron Laser, Photonics **7**, 125 (2020).

[16] G. D'Auria *et al.*, Status of the CompactLight Design Study, in *Proceedings of the 39th International Free Electron Laser Conference (FEL2019), Hamburg, Germany*, edited by W. Decking, H. Sinn, G. Geloni, S. Schreiber, M. Marx, and V. R. W. Schaa (JACoW, Geneva, Switzerland, 2019), THP078.

[17] A. Giribono *et al.*, Effects of mode launcher on beam dynamics in next generation high brightness C-band guns, in *Proceedings of the 12th International Particle Accelerator Conference (IPAC2021), Campinas, SP, Brazil* (JACoW, Geneva, 2021), MOPAB257.

[18] A. Giribono, A. Bacci, E. Chiadroni, A. Cianchi, M. Croia, M. Ferrario, A. Marocchino, V. Petrillo, R. Pompili, S. Romeo, M. Rossetti Conti, A. Rossi, and C. Vaccarezza, Eupraxialab: The high-brightness rf photoinjector layout proposal, Nucl. Instrum. Methods Phys. Res., Sect. A **909**, 282 (2018), 3rd European Advanced Accelerator Concepts workshop (EAAC2017).

[19] M. Ferrario *et al.*, Eupraxia@SPARC_LAB design study towards a compact FEL facility at LNF, Nucl. Instrum. Methods Phys. Res., Sect. A **909**, 134 (2018), 3rd European Advanced Accelerator Concepts workshop (EAAC2017).

[20] I.FAST—Innovation Fostering in Accelerator Science and Technology (I.FAST), https://ifast-project.eu/.

[21] M. Pedrozzi, SwissFEL Injector Conceptual Design Report, PSI Tech. Rep. No. PSI Bericht Nr. 10-04, 2010.

[22] T. Rao and D. H. Dowell, An engineering guide to photo-injectors, arXiv: 1403.7539.

[23] C. Ronsivalle, L. Giannessi, M. Quattromini, M. Ferrario, L. Ficcadenti, D. Filippetto, V. Fusco, B. Marchetti, M. Migliorati, A. Mostacci, L. Palumbo, C. Vaccarezza, A. Cianchi, A. Bacci, A. Rossi, and L. Serafini, Simulations of the emittance compensation in photoinjectors and comparison with sparc measurements short review of emittance, in *Proceedings of the 11th European Conference, EPAC 2008, Genoa, Italy*, edited by I. Andrian and C. Petit-Jean-Genaz (2008).

[24] C. Ronsivalle, L. Giannessi, M. Quattromini, M. Ferrario, L. Ficcadenti, D. Filippetto, M. Fusco, V. Boscolo, E. Chiadroni, D. Filippetto, G. Gatti, M. Migliorati, A. Mostacci, P. M., C. Vaccarezza, C. Vicario, A. Cianchi, A. Bacci, A. Rossi, and L. Serafini, Comparison between sparc e-meter measurements and simulations, in *Proceedings of the 2007 IEEE Particle Accelerator Conference (PAC), Albuquerque, NM* (IEEE, New York, 2007), pp. 986–988, https://dx.doi.org/10.1109/PAC.2007.4440957.

[25] K. Flöttmann, Astra: A space charge tracking algorithm (2011), http://www.desy.de/mpyflo.

[26] L. M. Young and J. Billen, The particle tracking code PARMELA, in *Proceedings of the 2003 Particle Accelerator Conference, Portland, OR, USA* (IEEE, New York, 2003), pp. 3521–3523, https://dx.doi.org/10.1109/PAC.2003.1289968.

[27] A. Bacci, V. Petrillo, and M. Rossetti Conti, GIOTTO: A Genetic Code for Demanding Beam-dynamics Optimizations, in *Proceedings of the 7th International Particle Accelerator Conference (IPAC 2016), Busan, Korea* (JaCow, Geneva, Switzerland, 2016), pp. 3073–3076, https://dx.doi.org/10.18429/JACoW-IPAC2016-WEPOY039.

[28] J. Scifo, A. Lorusso, E. Chiadroni, P. Cinquegrana, S. Dabagov, M. Danailov, A. Demidovich, M. Ferrario, D. Garzella, A. Giribono, D. Hampai, A. Perrone, and M. Trovò, Photoemission studies of yttrium photocathodes by using the visible radiation, Phys. Rev. Accel. Beams **23**, 123401 (2020).

[29] J. Scifo, D. Alesini, M. Anania, M. Bellaveglia, S. Bellucci, A. Biagioni, F. Bisesto, F. Cardelli, E. Chiadroni, A. Cianchi, G. Costa, D. Di Giovenale, G. Di Pirro, R. Di Raddo, D. Dowell, M. Ferrario, A. Giribono, A. Lorusso, F. Micciulla, A. Mostacci, D. Passeri, A. Perrone, L. Piersanti, R. Pompili, V. Shpakov, A. Stella, M. Trovò, and F. Villa, Nano-machining, surface analysis and emittance measurements of a copper photocathode at sparc_lab, Nucl. Instrum. Methods Phys. Res., Sect. A **909**, 233 (2018).

[30] Z. Zhang and C. Tang, Analytical study on emittance growth caused by roughness of a metallic photocathode, Phys. Rev. ST Accel. Beams **18**, 053401 (2015).

[31] D. Xiang, W.-H. Huang, Y.-C. Du, L.-X. Yan, R.-K. Li, C.-X. Tang, Y.-Z. Lin, S.-J. Park, and J. Park, First

principle measurements of thermal emittance for copper and magnesium, in *Proceedings of the 2007 IEEE Particle Accelerator Conference (PAC)* (IEEE, New York, 2007), pp. 1049–1051.

[32] R. W. Assmann, M. K. Weikum, T. Akhter, D. Alesini, A. S. Alexandrova, M. P. Anania, N. E. Andreev, I. Andriyash, M. Artioli, A. Aschikhin *et al.*, EuPRAXIA Conceptual Design Report, Eur. Phys. J. Spec. Top. **229,** 3675 (2020).

[33] A. Bacci, L. Faillace, L. Pellegrino, D. Alesini, S. Bini, F. Cardelli, G. Catuscelli, F. Chiarelli, I. Drebot, A. Esposito, A. Gallo, A. Ghigo, D. Giannotti, V. Petrillo, L. Piersanti, E. Puppin, M. Rossetti Conti, L. Serafini, A. Stella, A. Vannozzi, and S. Vescovi, STAR HE-linac complete detailed design report, arXiv:2109.10351.

[34] A. Bazzani, P. Cardarelli, G. Paternò, M. Placidi, A. Taibi, and G. Turchetti, Bocxs: A compact multidisciplinary x-ray source, Phys. Open **5,** 100036 (2020).

[35] E. Chiadroni, A. Cianchi, M. Ferrario, A. Mostacci, R. Pompili, and V. Shpakov, A versatile thz source from high-brightness electron beams: Generation and characterization, Condens. Matter **5,** 40 (2020).

[36] V. Dolgashev, High magnetic fields in couplers of *X*-band accelerating structures, in *Proceedings of the 2003 Bipolar/BiCMOS Circuits and Technology Meeting (IEEE Cat. No.03CH37440)*, Vol. 2 (IEEE, New York, 2004), pp. 1267–1269.

[37] D. Alesini, G. Castorina, M. Croia, M. Ferrario, A. Gallo, B. Spataro, C. Vaccarezza, and A. Vannozzi, Design of a full C-band injector for ultra-high brightness electron beam, Melbourne, Australia, in *10th International Particle Accelerator Conference (IPAC2019)* (JACoW, Geneva, 2019).

[38] A. Grudiev, S. Calatroni, and W. Wuensch, New local field quantity describing the high gradient limit of accelerating structures, Phys. Rev. ST Accel. Beams **12,** 102001 (2009).

[39] G. Castorina, L. Ficcadenti, M. Migliorati, A. Mostacci, L. Palumbo, F. Cardelli, G. Franzini, A. Marcelli, B. Spataro, G. Sorbello, L. Celona, S. Gammino, G. Torrisi, A. Cahill, J. Rosenzweig, and V. A. Dolgashev, A TM01 mode launcher with quadrupole field components cancellation for high brightness applications, J. Phys. Conf. Ser. **1067,** 082025 (2018).

[40] G. Pedrocchi, M. Migliorati, A. Mostacci, L. Palumbo, D. Alesini, A. Gallo, A. Giribono, B. Spataro, F. Cardelli, L. Ficcadenti, and G. Castorina, A C-Band rf Mode Launcher with Quadrupole Field Components cancellation for high brightness applications, in *10th International Particle Accelerator Conference (IPAC2021), Campinas, SP, Brazil* (JACoW, Geneva, 2021).

[41] D. Alesini, F. Cardelli, G. D. Raddo, L. Faillace, M. Ferrario, A. Gallo, A. Giribono, A. Gizzi, S. Lauciani, A. Liedl, L. Pellegrino, L. Piersanti, C. Vaccarezza, A. Vannozzi, M. Croia, G. Castorina, L. Ficcadenti, and G. Pedrocchi, The new C band gun for the next generation rf photo-injectors, in *11th International Particle Accelerator Conference (IPAC2022)* (2022).

[42] ANSYS Electronics Desktop website, https://www.ansys.com.

[43] Canon website, https://etd.canon/en/index.html.

[44] G. D'Auria, N. e. Thompson, J. e. Clarke, M. e. Ferrario, W. e. Wuensch, F. e. Nguyen, A. e. Aksoy, R. e. Rochow, A. e. Chianchi, A. e. Latina, and M. e. Aicheler, Xls—d2.3: Conceptual design report (2021), On behalf of the CompactLight Partnership—see list of all authors in the document.

[45] J. L. W. *et al.*, Reference manual for the POISSON/SUPERFISH Group of Codes, Tech. Rep. No. LA-UR-87-126 (1987).

[46] M. Diomede, D. Alesini, M. Bellaveglia, B. Buonomo, F. Cardelli, N. Catalan Lasheras, E. Chiadroni, G. Di Pirro, M. Ferrario, A. Gallo, A. Ghigo, A. Giribono, A. Grudiev, L. Piersanti, B. Spataro, C. Vaccarezza, and W. Wuensch, Preliminary rf design of an *X*-band linac for the EuPRAXIA at SPARC_LAB project, Nucl. Instrum. Methods Phys. Res., Sect. A **909,** 243 (2018).

[47] R. Zennaro, *C*-band rf pulse compressor for SwissFEL, in International Proceedings of the IPAC 2013, Shanghai, China (2013).

[48] T. Barts and J. Merson, User Notes for POISSON/SUPERFISH Release 3.0, Phys. Rev. ST Accel. Beams, LA-UR-91-4140.

[49] D. Palmer, X. Wang, I. Ben-Zvi, R. Miller, and J. Skaritka, Experimental results of a single emittance compensation solenoidal magnet, in *Proceedings of the 1997 Particle Accelerator Conference (Cat. No.97CH36167)*, Vol. 3 (1997), pp. 2843–2845.

[50] H. Busch, Berechnung der bahn von kathodenstrahlen im axialsymmetrischen elektromagnetischen felde, Ann. Phys. (Berlin) **386,** 974 (1926).

[51] A. Vannozzi *et al.*, Design and realization of new solenoids for high brightness electron beam injectors, in *Proc. 12th International Particle Accelerator Conference (IPAC'21), Campinas, Brazil* (JACoW, Geneva, 2021).